The LSST DESC Data Challenge 1: Generation and Analysis of Synthetic Images for Next Generation Surveys

J. Sánchez[1], C. W.Walter[2], H. Awan[3], E. Gawiser[3], A. Slosar[4], D. Kirkby[5], J. C. Chiang[6], T. Glanzman[6], S. F. Daniel[7], Y. AlSayyad[8], C. Burke[8], J. Cheng[8], S. Digel[6], R. Dubois[8], M. Jarvis[8], T. Johnson[8], H. Kelly[8], S. Krughoff[8], R. H. Lupton[8], R. Mandelbaum[8], P. J. Marshall[9], M. Mustafa[8], E. -H. Peng[8], J. Peterson[8], P. Price[8], G. Sembroski[8], B. Van Klaveren[8], M. Wiesener[8], B. Xin[8]

(LSST DESC Collaboration)

[1] *Department of Physics and Astronomy, University of California, Irvine, Frederick Reines Hall, Irvine, CA, U.S.A.*
[2] *Duke University, Department of Physics, Durham, NC, U.S.A.*
[3] *Department of Physics & Astronomy, Rutgers, The State University of New Jersey, 136 Frelinghuysen Rd, Piscataway, NJ U.S.A.*
[4] *Brookhaven National Laboratory, Upton, NY, U.S.A.*
[5] *Department of Physics and Astronomy, University of California, Irvine, Frederick Reines Hall, Irvine, CA*
[6] *SLAC National Accelerator Laboratory,2575 Sand Hill Rd, Menlo Park, CA, USA*
[7] *Department of Astronomy, University of Washington, Seattle, WA, USA*
[8] *Affiliation*
[9] *Kavli Institute for Particle Astrophysics & Cosmology, P. O. Box 2450, Stanford University, Stanford, CA, USA*

8 April 2018

ABSTRACT

The success of the Large Synoptic Survey Telescope (LSST) as a dark energy experiment will depend on controlling systematic effects for the various cosmological probes. Simulations are critical for developing the methodology to estimate and mitigate these systematics. In the first Data Challenge from the LSST Dark Energy Science Collaboration, we evaluate the potential systematic effects that will affect observables, with an emphasis on galaxy clustering. We utilized two approaches to simulate LSST images, one of which involves fully realistic ray-tracing. Simulated images were then processed, combined, and analyzed using the current version of the LSST Data Management pipeline. Here we characterize the resulting systematics and implement corrections. Our results demonstrate that we can generate realistic LSST-like simulated images and control the systematic effects, after processing these images, at a sufficient level to enable major advances in our knowledge of dark energy and cosmology. The methodology presented here can be easily translated to current and future imaging surveys.**Rewrite**

Key words: LSS , Data challenge, Systematics

1 INTRODUCTION

The increase in statistical power from recent cosmological experiments makes the modeling, and mitigation of systematic uncertainties key to extract the maximum performance and produce competitive analyses. More traditional in high energy particle physics (Brun et al. 1978), (Sjöstrand et al. 2006), end-to-end simulations provide a unique framework to model systematics and streamline processing and analysis pipelines given that we have complete information about the inputs and outputs. With the larger availability of computational resources this approach has also been extended to

photometric redshift galaxy surveys (Suchyta et al. 2016; Bruderer et al. 2016), and a similar effort is undergoing in spectroscopic surveys such as DESI (DESI Collaboration et al. 2016). For surveys like the LSST (Ivezic et al. 2008b), where the expected data volume is very large, and where a highly stringent control of the systematic uncertainties is required, producing these kind of end-to-end simulations becomes necessary. With ~ 50 PB of raw data and ~ 40 billion objects (Ivezic et al. 2008b) the data handling by itself becomes challenging. There are many approaches to generate these end-to-end simulations. Usually, one would start from a source catalog with sources parametrized somehow

(*e.g.* sizes, shapes, fluxes), render images from these sources, adding some observational effects and, finally, use some software to detect and measure different properties on these images. Depending on the approach used to generate these images, some difficulties may arise when trying to relate inputs and outputs, especially, in a situation like LSST with its large data volume.

In this paper, we use simulated images that resemble the data that will be produced by LSST (Ivezic et al. 2008b) after 10 years of operation in r-band using state of the art tools. We characterize the products of this process, measuring photometric, astrometric and clustering properties of the sample. These products encompass single-visit and coadded calibrated exposures (i.e., flattened, background subtracted, etc) and source catalogs that add up to $\sim 225TB$. They are the result of two different simulations that will be introduced later.

This paper is structured as follows: In Section 2 we describe the inputs for our simulated images. In Section 4 we describe the process to generate our LSST-like artificial images. Finally, in Section 9 we present some concluding remarks.

2 IMAGE GENERATION: INPUT CATALOG

Please, Daniel and/or Simon check this Image simulations can give very valuable information about the detection and deblending process and about instrumental and astrophysical systematics. For example, if we generate a catalog with random positions uniformly distributed across the sky, as well as uniformly random shapes and fluxes, we can get information about detection efficiencies as a function of flux but, the information about blending will definitely not be realistic, and we will not able to capture some correlations present in real data. However, using a N-body simulation as the input to generate artificial images allows us to study all the aforementioned effects. This is why we used the `CatSim` Reference? catalog as our input. This catalog uses the dark matter haloes from the Millennium simulation (Springel et al. 2005) and a semi-analytic baryon model described in De Lucia et al. (2006). The semi-analytic model features radiative cooling, star formation, the dynamics of black holes, supernovae, and AGNs and was adjusted to mimic the luminosity, color, and morphology distributions of low redshift galaxies. `CatSim` was generated by constructing a lightcone, covering redshifts $0 < z < 6$ from 58 500 $h^{?1}$ Mpc simulation snapshots. The final catalog comprises a 4.5×4.5 degree footprint on the sky (sufficient to cover a single LSST field-of-view) and samples halo masses over the range 2.5×10^9 to 10^{12} $M_{\odot}$.I copied this from https://www.lsst.org/scientists/simulations/catsim, is that fine?

For DC1, this catalog was tiled to generate a ~ 40 deg^2 footprint. This approach introduces some periodicity that induces some spurious correlations in our sample, however, we checked that these effects appear at large scales larger than we are able to map given the DC1 area. For all sources, a spectral energy distribution (SED), is fit to the galaxy colors using Bruzual & Charlot (2003) spectral synthesis models. The De Lucia et al. (2006) catalog includes BVRIK magnitudes and dust values for the disk and bulge compo-
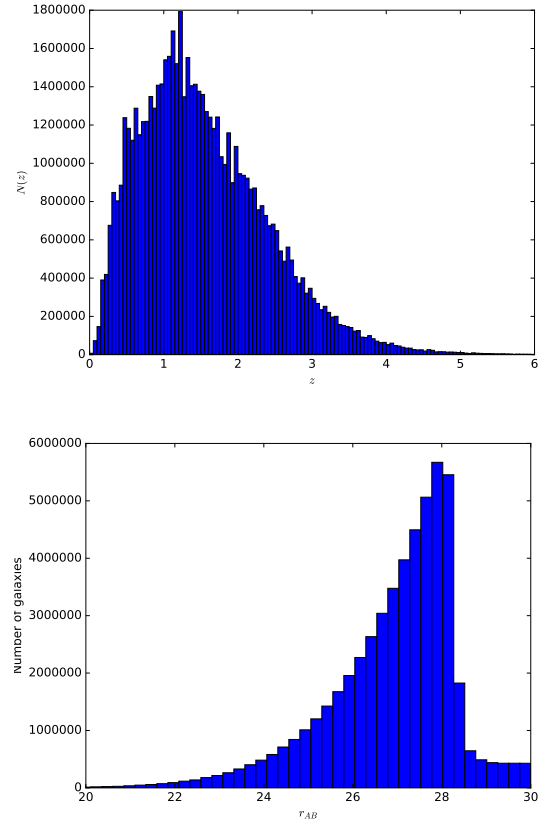
Figure 1. Redshift (top) and magnitude (bottom) distribution for the galaxies used as inputs for DC1.

nents of each galaxy as well as radii, redshift, coordinates, stellar age, masses and metallicities. Fits are undertaken independently for the bulge and disk and include inclination dependent reddening. Morphologies are modeled using two Sérsic profiles (Sérsic 1963) and a single point source (for the AGN). Bulge-to-disk ratios and disk scale lengths are taken from (De Lucia et al. 2006). Half-light radii for bulges are derived from the absolute-magnitude vs half-light radius relation given by Gonzalez et al. (2011). Colors and stellar mass of the AGN host galaxies are estimated from the AGN luminosities.

Stars are represented as point sources and are drawn from the Galfast model (Jurić et al. 2008). Galfast generates stars according to density laws derived from fitting SDSS data to a model of a thick and thin disk, and a halo. Each star is assigned a metallicity, proper motion, and parallax.

In total, the input catalog contains approximately 63.1 million sources of which, 61.3 million are galaxies whose redshift and magnitude distributions are depicted in Figure 1 and 1.8 million are stars. Using this catalog we generate images covering an area of approximately 40 square degrees (4 pointings) in r-band to LSST full depth (10 years). The final footprint can be seen in Figure 2

3 DITHERING STRATEGY

Please, Humna and/or Eric check this section.
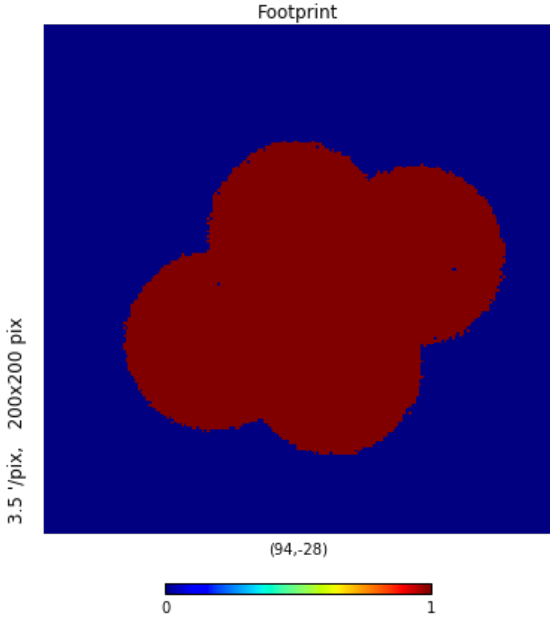
Figure 2. Footprint of the DC1 dataset. We simulate 4 LSST full focal plane pointings which roughly corresponds to 40 square degrees.

Different dithering strategies affect differently to the survey uniformity and systematic effects in photometric redshift surveys (Awan et al. 2016). Simulating two different strategies is beneficial to check which can be more effective to mitigate systematic effects and yield better cosmological constraints. For this data challenge we use two different dithering strategies: the *undithered* which consists just on point the telescope with the same position and orientation in all exposures; and the *dithered* which consists in small random rotational and translational dithers for each pointing/exposure. This dithering strategy is stored in the `minion_1016_new_dithers` OpSim[1] database presented in ref. (Awan et al. 2016). However, with dithering, we might have some visits where part of the focal plane lies outside of our region of interest. In order to save computational resources, we decided not to simulate those exposures since the depth and uniformity would have been lower than in our region of interest and would be discarded for most analyses anyway.

4 IMAGE GENERATION: PIPELINE

The artificial generation of astronomical images is a complex and computationally demanding process. In the recent years there is a big effort in the community in order to create software that allows more realistic and fast image generation (Suchyta et al. 2016; Bruderer et al. 2016). In our case, we model the input sources using imSim which uses GAL-SIM (Rowe et al. 2015) as a library driven by a LSST specific

application. There are other approaches consisting in running a full photon-shooting simulation using PHOSIM (Peterson et al. 2015). This approach will be used in future Data Challenges. The former has a speed advantage but the latter fully traces each photon coming from the sources through the atmosphere and the instrument, increasing the level of realism with a fairly high computational cost. These two approaches can potentially allow us to focus on different systematic effects and science cases.

4.1 imSim

imSim follows the path of the fast image simulations in refs. (Suchyta et al. 2016; Bruderer et al. 2016). imSim uses GALSIM (Rowe et al. 2015) to generate images that resemble LSST individual visits. Instead of the planned two 15 seconds exposures planned (Ivezic et al. 2008b) we generate a single 30 seconds image to speed up the process. We simulate each CCD of the focal plane individually but there are no instrumental effects nor variability in the optical model across the focal plane except for the sky. We used an ESO sky model and the sky brightness values come from OpSim reference?[2] and we add the corresponding noise using GALSIM. The PSF model that we use is a Gaussian for the system with a FWHM that depends on the airmass [3] plus a Kolmogorov profile to model the atmosphere that is airmass dependent as well [4]. The airmass model is taken from (Krisciunas & Schaefer 1991);

$$X = (1 - 0.96 \sin Z)^{-0.5}, \tag{1}$$

where X is the airmass, and Z the angular distance to the zenith.

In this simulation we can find three different types of objects: Stars which are modeled as a very narrow Gaussian profile with $\sigma = 10^{-8}$ Check this!; galaxies, which are modeled as Sérsic profiles (Sérsic 1963) (bulge plus disk) using the parameters given by CatSim; and AGNs that are also modeled as very narrow Gaussian profiles. In this version of the catalog we decided to not include variability in AGNs to simplify the analysis. The zeropoints are computed using the model presented at (Ivezic et al. 2008b) and the throughputs at `https://github.com/lsst/throughputs`. We clip the objects at magnitude 10 to simulate saturation.

The final products of this pipeline are FITS images with information about the observing conditions as expected by the LSST software stack. We generated more than 200,000 images in total (including both the *dithered*, and *undithered* fields). The typical time to simulate each CCD is seconds.

4.2 Image processing pipeline

The outputs of these simulations are then processed using the LSST data management (DM) stack (Ivezic et al. 2008a; LSST Science Collaboration 2009; LSST Dark Energy Science Collaboration 2012; Bosch et al. 2017; Jurić et al. 2015) . This is an open source high-performance data processing and analysis system intended for use in O/IR

---

[1] `https://www.lsst.org/scientists/simulations/opsim`

[2] We used the values at OpSim's run `minion_1016`
[3] From LSST-20160 eqn. (4.1)
[4] From LSST-20160 eqn. (4.2)
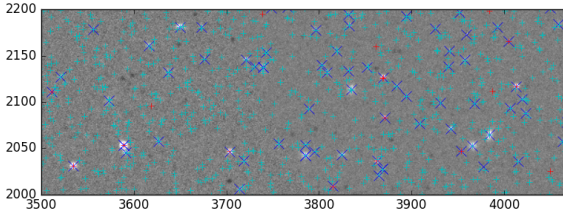
Figure 3. Example of a 550×200 pixel simulated field. The axes show the pixel number in the CCD. The input galaxies are marked with cyan +, the input stars are marked with red +, and the detected sources are marked with blue ×. We can appreciate the vast difference in density between the simulation and the output given that CatSim contains objects fainter than what LSST can detect.

survey data. The code can be found at `dm.lsst.org` and `pipelines.lsst.io`. The raw, uncalibrated single exposures are used as inputs. The software performs the reduction, detection, deblending and measurement on individual visits and coadds producing the level 2 data products (Jurić et al. 2015). Although it is still under development, most of the pieces are already meeting the science requirements or very close to do that. Running the DM stack on this dataset also constitutes a necessary test for this invaluable piece of LSST. The DM stack performs these provides calibrated images and a source catalog with ~ 10.6 million objects with position, flux and shape information.

An example of a coadd image can be seen at Figure 3.

5 OUTPUT CATALOGS

After being processed, the catalogs are accessible by DESC collaborators and stored at NERSC. We generate `pandas dataframes` and databases for each one of the coadd and input catalogs in order to be accessed by the collaborators and perform their own analyses. The output catalogs contain 10.6 million objects covering an area of ~ 43 deg^2. The catalogs include information about position, size, shape and magnitude for every object. They include several flags that give information about the presence of interpolated/saturated pixels in the objects or whether these objects are close to the edge of a CCD or not.

In order to check the level of realism and the accuracy of the processed catalogs we perform several quality assurance tests.

5.1 Astrometry checks

Biases in astrometry can potentially affect both clustering and weak lensing measurements. These biases can have different origins: PSF mis-characterization, non corrected sensor effects, incorrect modeling of proper motion for the measured objects and presence of blended sources are among the most common sources.

We will follow two approaches to check the quality of the astrometric solutions that we obtained: an *external* check

comparing to the input *truth* catalog; and an *internal* check comparing different visits.

5.1.1 External checks

As we have already mentioned, one of the big advantages of using simulations is that we have access to the *true* underlying information. We will use this information to check the precision of the astrometric measurements in single exposures and co-adds. For these studies we will select stellar objects. In order to do so, we use the classifier included in the LSST software stack[5] and choose objects with `base_ClassificationExtendedness_value==0`. We also require that `deblend_nChild==0` to ensure that the objects are completely deblended, i.e., they are primary sources. We match these objects to the stellar sources in the input catalog. In both cases we will use a `KDTree` (Pedregosa et al. 2011) to retrieve those objects in the input catalog that are in a radius of 0.2 arc-seconds (one pixel) of those detected in the output catalog and select the match that is closest in magnitude. We only consider sources which have a magnitude difference smaller than 0.02 magnitudes. We will discuss matching strategies deeper in Section 6.

We selected a representative single visit (visit number 270675 for the imSim dithered run) and calculated the difference between the measured and the input positions. These are represented in Figure 4. We can see that both RA and Dec distributions are compatible with each other, meaning that there are no anisotropies in the detection, as expected from the inputs. However, we find that the distributions are asymmetric and that the median is not zero. This effect is even more noticeable when we accumulate visits as in Figure 5, where we accumulated the results for 50 randomly selected visits of the imSim dithered run. This effect is also present in the dithered and undithered imSim runs and in the PhoSim run. We also checked the dependence the mean astrometric residual with the magnitude of the objects as shown in Figure 5 where a mild bias for the brightest objects can be seen. This bias is smaller than 15 mas, much smaller than the resolution of the input N-body simulation. This means that the two point clustering statistics will not be affected by this bias. This bias arises from the fact that the objects in the images include proper motion which is unaccounted for in our *truth tables*.

We also wanted to check if there is a preferred orientation for the differences between the input and output position in a single visit. Using the same visit as before we show the astrometric residuals in Figure 6. In this Figure we can see that the astrometric residuals do not show any noticeable structure and appear to be mostly random with the largest contributions close to the CCD edges.

5.1.2 Internal checks

Another important test is to ensure the internal consistency of the astrometric solutions between different exposures. To do that we selected a small region of the co-added area (*patch*) and compared the positions of the objects detected

---
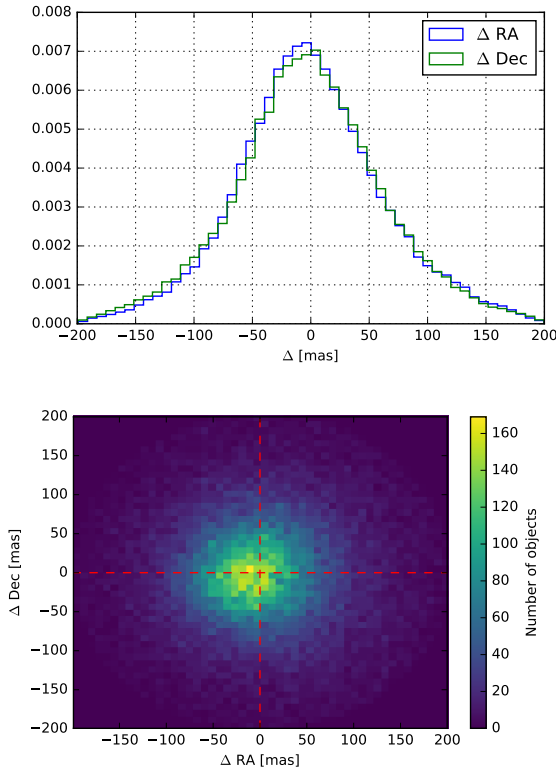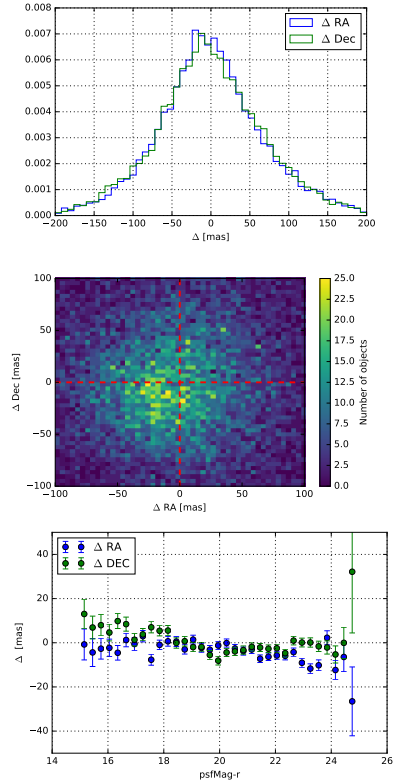
Figure 4. Left: Distribution of the difference $\Delta = X_{measured} - X_{input}$ in RA (blue) and Dec (green) coordinates. We cannot appreciate any differences between these, however we see that there is median is not at zero $\Delta_{median} \approx -2$ mas. The histograms are normalized such that the total sum of the counts is equal to one. Right: 2D histogram showing the bivariate distribution of the difference in RA (horizontal axis) and Dec (vertical axis). We selected one random representative exposure (visit number 270675 for the imSim dithered run). The effect is similar for the undithered imSim run and for the PhoSim run.

Figure 5. Left: Distribution of the difference $\Delta = X_{measured} - X_{input}$ in RA (blue) and Dec (green) coordinates as in Figure 4 but accumulating the results for 50 randomly selected visits from the imSim dithered run. Middle: 2D histogram showing the bivariate distribution of the difference in RA (horizontal axis) and Dec (vertical axis). Right: Mean astrometric residual as a function of magnitude for RA (blue) and Dec (green). These distributions are similar for the undithered imSim run and for the PhoSim run.

in the co-add image with the positions of objects detected in individual exposures that overlap with that patch.
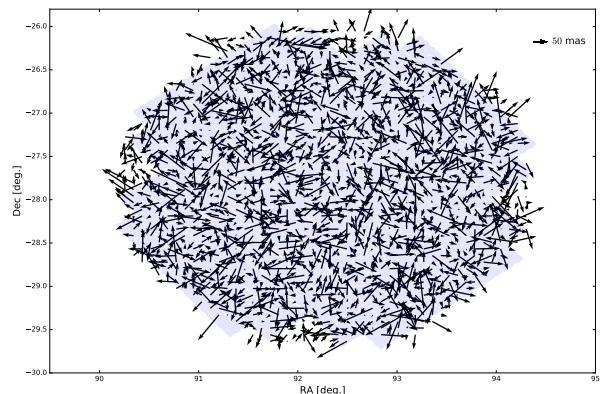
In particular, we randomly chose 10 catalogs from individual exposures and looked for objects that fulfilled the following criteria:

- `deblend_nChild==0`, this means that the object has been completely deblended (it is a primary match).
- `base_PixelFlags_flag_edge==0`, which means that the object is not close to an edge.
- `base_PixelFlags_flag_interpolatedCenter==0`, the object does not have any interpolated pixels in its center.

Note that in this case we are not requiring the objects to be classified as stars (we are omitting the cut in `base_ClassificationExtendedness_value`) but we are adding some cuts to ensure that the objects were properly measured. Once we perform our selection, the next step is to match the objects in the different exposures. To do so we use the matching algorithm included in the LSST software stackReference? and calculate the mean of the difference between the position of each source in the co-add, $X_{coadd,i}$ and

Figure 6. Astrometic residuals measured in visit 270675 from the imSim dithered run. The light blue squares represent the CCD chips in the LSST focal plane. The base of the arrow is on the input matched object. The arrows have been re-scaled 10,000 for visualization purposes.
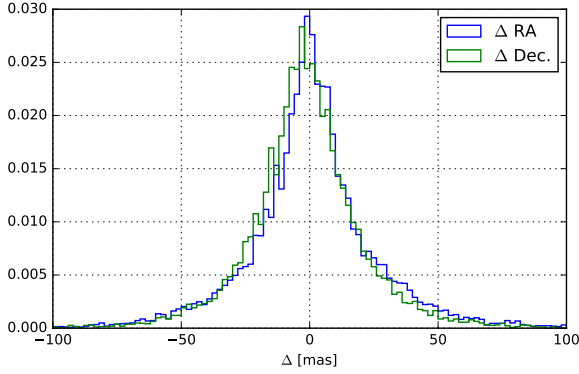
Figure 7. Distribution of the mean difference in position (RA:blue, Dec:green) between the coadd and the different individual exposures where each source has been detected.

the position of the matched object in each of the exposures where it has been detected, $X_{visit_j,i}$ for $j \in [1, 10]$, i.e,

$$\Delta = \langle X_{coadd,i} - X_{visit_j,i} \rangle \qquad (2)$$

we only consider sources that have been detected in at least 5 exposures. The resulting distribution is shown in Figure 7 where we see that is noticeably narrower than those shown in Figure 4 and Figure 5 and no apparent bias is found showing that the processing is consistent.

5.2   Photometry checks

As we did in previous sections we are going to perform two different tests to test the quality of our simulations: first we are going to compare our output catalogs to the inputs, and second we are going to check the consistency between different visits for the same objects.

5.2.1   External checks

We want to analyze the accuracy of the magnitude measurement comparing the input catalog with the output image. This process not only checks the accuracy of the measurement pipeline but also, it tests the quality and level of realism of the image generation pipeline. For these external checks we use again the same 50 randomly selected visits as we did in the previous section to check the astrometric residuals. To study the photometric residuals we change slightly the matching strategy from previous sections. In this case we eliminate the threshold in magnitude difference so, we just look for the input source that is closest in magnitude in a 0.2 arc-seconds radius around each detected source. In Figure 8 we can see the distribution of the photometric residuals. We see that this distribution gets wider as we go fainter (as expected) and that the 0.02 magnitude selection cut was a good proxy to ensure that we account for most sources properly matched.

5.2.2   Internal checks

We also checked the consistency of the photometry between different exposures. Using the same approach and sample
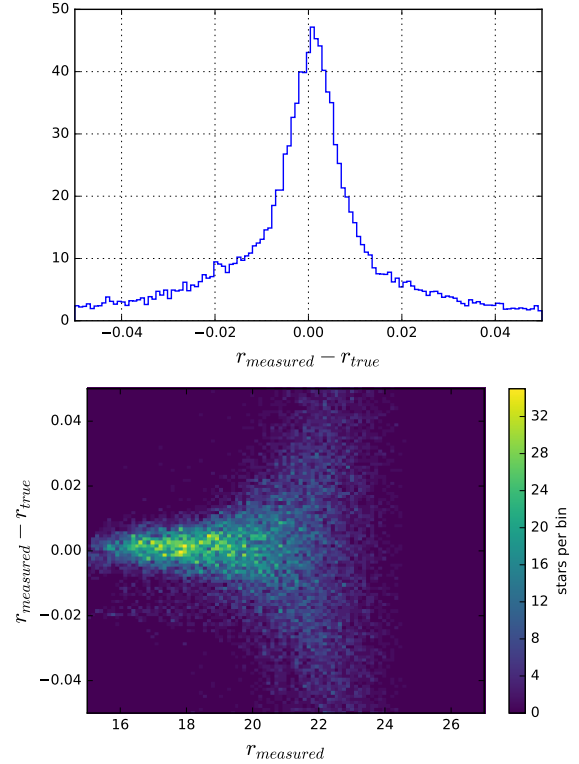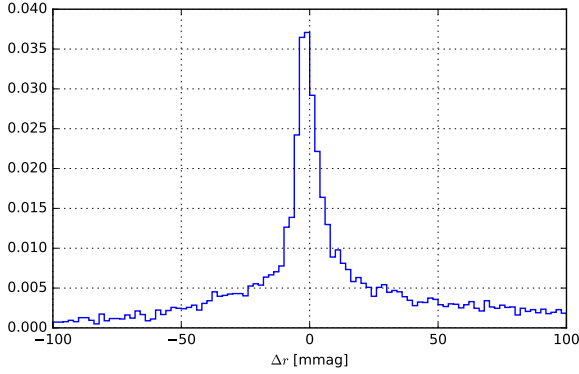

Figure 8. Left: Distribution of magnitude difference between the input and output catalogs. Right: Difference magnitude between input and output catalogs as a function of the measured magnitude. We considered 50 visits randomly selected from the imSim dithered run. We find similar results for the imSim undithered run and for the PhoSim run.

presented in Section 5.1.2 we compared the mean difference between the coadded source and 10 random single-visit images. In principle, we would expect that some objects will show differences between different epochs due to their intrinsic variability, however, these effects are not found in the inputs of the simulation for any of the objects, thus, the differences between different epochs will come mainly from statistical fluctuations and different observing conditions. The results from these checks can be seen in Figure 9.

In this Figure we can see that the mean of the distribution is compatible with zero and that most sources have a magnitude difference lower than 25 mmag given the narrow peak. However we can appreciate the presence of long tails probably due to blends and mismatching or artifacts.

5.3   PSF checks

In order to ensure the accuracy of shape measurements a robust and accurate estimation of the PSF is required. In the case of imSim, we have a perfectly known input PSF that only depends on the airmass at the time of observation. We can check if the measurement pipeline can reconstruct the PSF and at which level of precision. To do that, we select 50 randoms visits, retrieve the measured PSF using the pipeline, and compare this to the input model given the

Figure 9. Distribution of the mean difference in magnitude between the coadd and the different individual exposures where each source has been detected. The mean of the distribution is consistent with zero.

observing conditions and compute the residual.Include the PSF results!!!!

6 MATCHING INPUT AND OUTPUT CATALOGS

Potentially, in end-to-end simulations, one can trace back each measured photon to its corresponding source in order to characterize the measurement process. However, this is not always possible for several reasons. For example, a simple solution could be storing each postage stamp for the different sources in different exposures. The problem with this approach is that it creates a large overhead in an already big dataset. Generating efficient strategies to perform this bookkeeping and connecting input and output catalogs is then, an important research topic for these kinds of end-to-end simulations.

The simplest way to connect two catalogs is by using the positions of the objects in the sky. This approach has been extensively used in the literature and performs reasonably well when blending is low, since the probability of confusing two objects is small. However, when blending is high, this approach might be not enough and matching other quantities like flux or shape can become useful, even though these can introduce some subtleties, an example being, how to weigh positions versus fluxes (and/or shapes) and whether or not we should consider the correlations between the two.

7 GENERATING DEPTH MAPS

In order to estimate the depth in the coadd catalogs we select the stars by using `base_ClassificationExtendedness_value==0`. This ensures selecting PSF-like objects. After this, we have two different approaches:

(i) In the first approach we generate a HEALPix (Górski et al. 2005) map containing the PSF-like objects detected with a signal-to-noise ratio (SNR) higher or equal than 5 (`base_PsfFlux_flux/base_PsfFlux_fluxSigma>=5`), and we

assign to each pixel the value of the dimmest object contained in it.

(ii) The second procedure also generates a HEALPix (Górski et al. 2005) map containing the PSF-like objects. Then in each pixel, we compute the median SNR as a function of the magnitude and get the magnitude at which SNR is the closest to 5.

These two procedures yield very similar results (within $\sim 4\%$) as it can be seen in Figure 10. We checked that the maps built selecting galaxies instead of stars are compatible as well. We will select our footprint according to the depth map using the second methodology which can be seen in Figure 11.

7.1 Bright objects masking and data selection

Bright objects produce significant effects in the image that affects the detection and measurement of neighboring objects. Some examples of the effect of these objects are: saturation of the CCD, large diffraction spikes, obscuration of neighboring sources, etc. Thus, masking a region around these sources makes a more complicated footprint but largely simplifies the analysis of systematic effects. In order to evaluate the effect of this sources, we use the stars from the input catalog, we divide them in different magnitude bins, and we count the detected objects in a given radius. However, the number of objects in a given radius is dependent of the number of stars in each bin and subject to statistical fluctuations. Therefore, we use instead the average on this number for the different magnitude bins. This analysis is largely simplified if we use the numerical derivative of this quantity. In Figure 12 we can see that there is an excess of sources at distances lower than 10 arcseconds for the brightest stars. This is mainly due to the existence of fake sources around these bright objects. The brighter sources also have a larger noise, the DM deblender models the brightest source and subtracts this model looking for fainter sources that can be blended together with it. However, sometimes there are large noise peaks that have not been subtracted. These large noise peaks are detected in later stages as individual (point-like) sources giving as a result these fake sources. However, we do not see any obscuration present at the scales that we are interested (1 arcmin and higher) so it seems that no masking is required but we need to select the objects for our analysis carefully.

We checked the detection efficiency of galaxies in our sample. In order to do so we selected galaxies in the catalog using the variable `base_ClassificationExtendedness_value` as a star/galaxy separator as in ref. (Bosch et al. 2017). Objects where this variable is 1 are more likely to be galaxies, whereas the objects where it is 0 are more likely to be stars. We also made some quality cuts by selecting the objects with `detect_isPrimary==True`. This ensures that the object has been fully deblended and that the detection was not close to the edge of a coadded image. The results can be seen in Figure 13 where we computed the ratio o of detected objects classified as galaxies and the input number of galaxies, ε as a function of magnitude. We checked this ratio for both the dithered and undithered catalogs and in pixels where the depths were higher than 25.7 and 26.25.
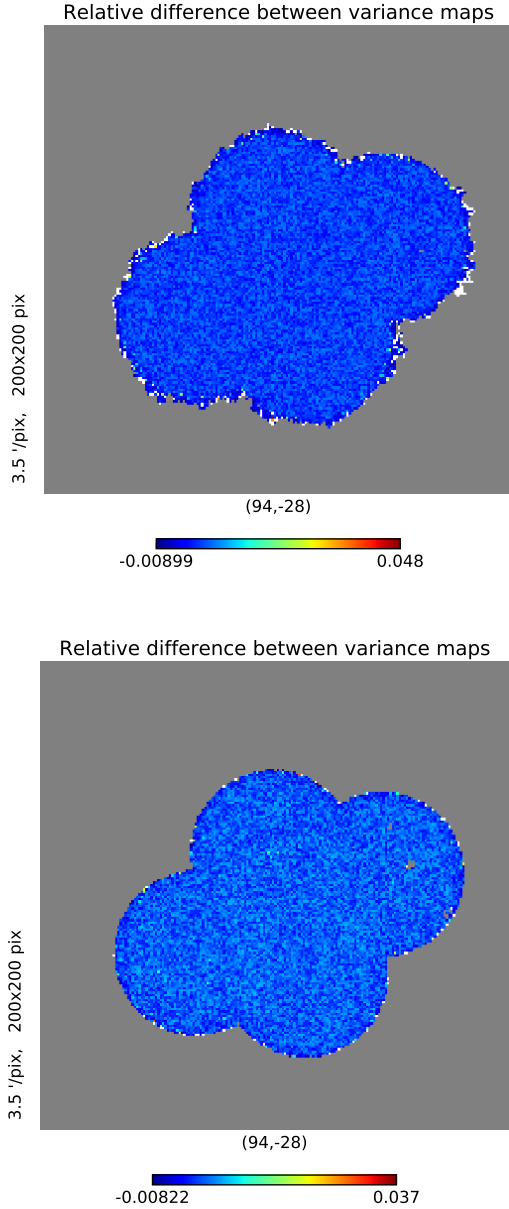
Figure 10. Relative difference between the depth calculated using the two methods presented in the text for the dithered (top) and undithered (bottom) fields.

Figure 11. 5-σ depth for the dithered (top) and undithered (bottom) fields.

We used `CMODEL_MAG` (see ref. (Bosch et al. 2017) for more details) as the reference magnitude for the detected objects and the true magnitude for the input galaxies.

Looking at Figure 13 it seems that selecting galaxies with `base_ClassificationExtendedness_value==1`, `detect_isPrimary==True` and `CMODEL_MAG > 21` is enough to get rid of most potential problems with fake detections. On top of that, it seems that selecting `CMODEL_MAG < 25.3` ensures good level of completeness ($\sim 80\%$). Uniformity is ensured by selecting the galaxies that lie within HEALPixels where the depth is greater or equal than 25.3. After these selection cuts we end up with 4.4 million galaxies for the dithered field and 4.3 for the undithered field.
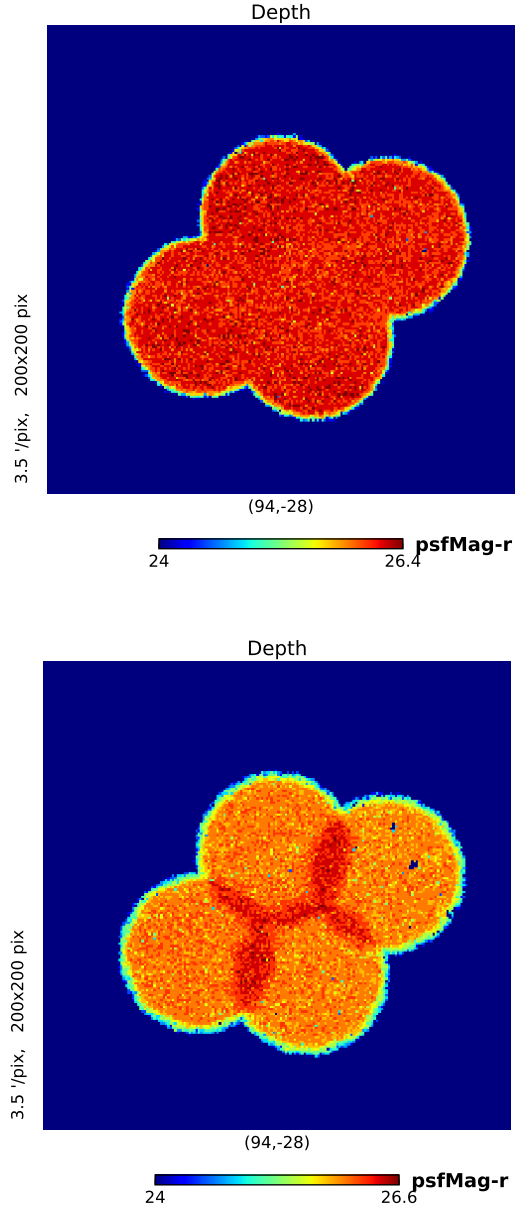
8   CLUSTERING RESULTS

In this section we analyze the two point clustering statistics for both the dithered and undithered catalogs in real and harmonic space and check the consistency between the input and measured observables. When comparing the input and output catalogs some subtleties arise. Let us think of a galaxy that has been measured with magnitude m_{meas} and with true magnitude m_{true} and we choose a magnitude threshold $m_{threshold}$ to define the sample of interest. If the luminosity function were flat, and assuming that the errors in magnitude are symmetric (which is not true) we would have as many objects with $m_{meas} < m_{threshold}$, but $m_{true} > m_{threshold}$ as objects with $m_{meas} > m_{threshold}$ but $m_{true} < m_{threshold}$, and this wouldn't change very much the
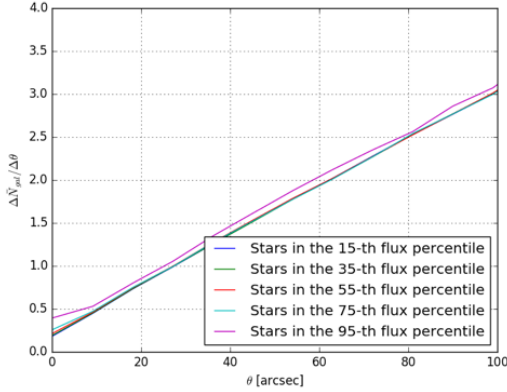
Figure 12. Mean increment in the number of detected objects around stars in the 95th flux percentile (magenta), the 75th percentile (cyan), the 55th percentile (red), the 35th percentile (green) and the 15th percentile (blue). We see that for the brightest percentiles there is no obscuration present but a overdensity of targets. These are mainly noise peaks identified as point sources.
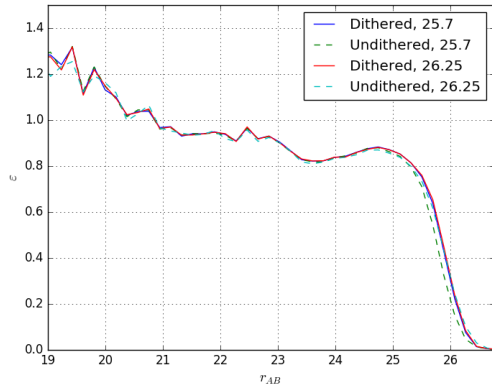
Figure 13. Number of detected objects classified as galaxies divided by the number input galaxies as a function of magnitude. We see that the detection efficiency is larger than 80% for the most part and a considerable fraction of objects with magnitude lower than 20 are being misclassified.

clustering properties of our sample and we could just compare directly the samples using the magnitude threshold in true magnitude and measured magnitude. However, this is not the case, given that the luminosity function is a growing function with magnitude, we expect more objects with $m_{meas} < m_{threshold}$, but $m_{true} > m_{threshold}$ than objects with $m_{meas} > m_{threshold}$ and $m_{true} < m_{threshold}$. So, in our measured sample we have more galaxies than in the sample selected with the true magnitude with the same magnitude threshold.

8.1 2-point correlation function

Using the samples presented in previous sections, we measure the 2-point correlation function using the package

TreeCorr (Jarvis et al. 2004) with the Landy & Szalay estimator (Landy & Szalay 1993).

$$w(\theta) = \frac{DD - 2DR + RR}{RR} \tag{3}$$

where DD, DR, and RR are the number of pairs of objects taking from the data D or the random catalog R that covers the footprint. We use 15 angular log-spaced bins between $\theta = 0.05°$ and $\theta = 10°$. The number of bins has been chosen so that the resulting covariance matrix is nearly diagonal. The covariance matrices are calculated using the delete-one jackknife technique (Shao 1986; Norberg et al. 2009). We divide the footprint in $N_{JK} = 100$ regions. These regions are defined using the K-means algorithm from the package kmeans_radec[6]. The covariance matrix is then computed as

$$\mathrm{Cov}_{JK}(\theta_i, \theta_j) = \frac{N_{JK} - 1}{N_{JK}} \sum_{k=1}^{N_{JK}} \Delta w_k(\theta_i) \Delta w_k(\theta_j) \tag{4}$$

$$\Delta w_k(\theta_i) = w_k(\theta_i) - \bar{w}(\theta_i) \tag{5}$$

Where $w_k(\theta_i)$ is the value of the correlation function when deleting the k-th region at the scale θ_i, and $\bar{w}(\theta_i)$ is the average correlation function at that same scale. We compute the correlation function on the dithered and undithered catalogs using their respective footprints, and we compare with the truth catalog in the dithered footprint using the same magnitude cuts. The results can be seen at Figure 17.

We also show the correlation matrix,

$$\mathrm{Corr}_{ij} = \frac{\mathrm{Cov}_{ij}}{\sqrt{\mathrm{Cov}_{ii}\mathrm{Cov}_{jj}}} \tag{6}$$

in Figure 14 where we can see that in both cases the matrices are almost diagonal.

8.2 Angular power spectrum

We measure the angular power spectrum using the NaMaster[7] package. This package computes the cross-power-spectra of masked fields with an arbitrary number of contaminants using a pseudo-C_ℓ approach (Hivon et al. 2002; Elsner et al. 2017). As we do for real space, we select the number of ℓ bins so that the covariance matrix is almost diagonal. In this case we calculate the power spectrum in the range $0 < \ell < 2000$ and $\Delta\ell = 75$. We calculate the covariance matrices with two different approaches: One consists in the same delete-one jackknife technique performed in real space; in the other approach we compute the Gaussian covariances (Dodelson 2003; Cabré et al. 2007)

$$\mathrm{Cov}_{\ell\ell'} = \frac{2}{f_{sky}} \left(\frac{C_\ell^2}{2\ell + 1} + \frac{1}{\bar{n}^2} \right) \delta_{\ell\ell'} \tag{7}$$

where $\bar{n}$ is the number density (objects per steradian). We compute the theoretical prediction for the power-spectra

---

[6] https://github.com/esheldon/kmeans_radec
[7] https://github.com/damonge/NaMaster
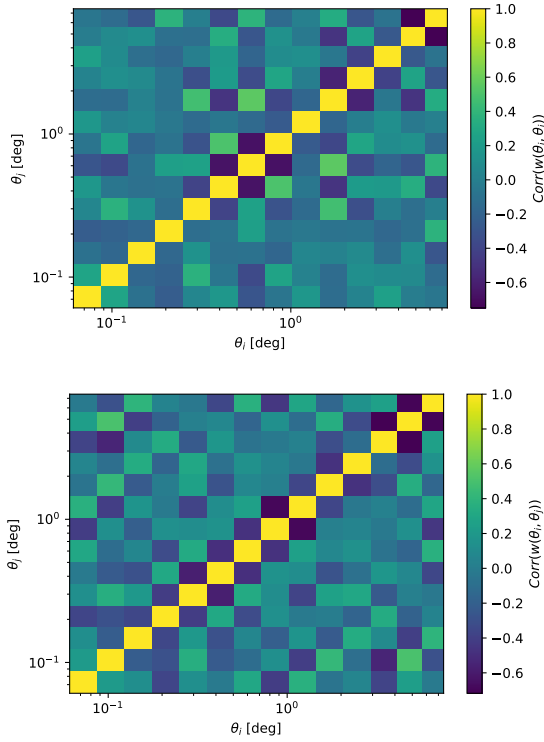
Figure 14. Correlation matrices for the dithered (top) and undithered catalogs (bottom).

with `CCL`[8] and use them to calculate the covariance matrices given that the predictions are noise-free.

$$C_\ell^{TH} = \frac{2}{\pi} \int dz \left(\frac{dn(z)}{dz}\right)^2 b^2(z) \int dk k^2 P(k,z) j_\ell^2(kr(z)) \tag{8}$$

Where $P(k,z)$ is the power spectrum, $b(z)$ is the bias and $\frac{dn}{dz}$ is the number density as a function of redshift. We use the Millenium cosmological parameters (Springel et al. 2005) ($\Omega_m = 0.25$, $\Omega_b = 0.045$, $\Omega_\Lambda = 0.75$, $n = 1$, $\sigma_8 = 0.9$, $h = 0.73$), and the $\frac{dn}{dz}$ built with the input catalog using the same magnitude cuts. The results can be seen in Figure 15. It seems that there is a small bias between the measured power-spectra and the input data power-spectrum (and between the dithered and undithered data), however, the error bars in the data are large enough to make this bias negligible.

8.3   Systematic effects

In this section we analyze the different systematic effects affecting the DC1 data. We will consider the following observational quantities as sources for systematic uncertainties:

- Extinction: The CatSim catalog provides the value for the magnitudes already corrected for extinction using the SFD map (Schlegel et al. 1998). We use this map to cross-correlate with our galaxy catalogs.

8 https://github.com/LSSTDESC/CCL
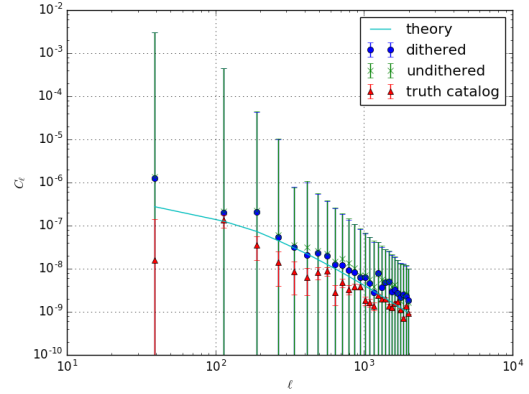
Figure 15. Measured power spectra for the input (red), undithered (green) and dithered (blue) datasets with `NaMaster`. The error bars are computed using the Gaussian approximation. All datasets seem to be compatible with the theoretical prediction (cyan) within 1-σ.

- Stellar contamination: In this case we just build a HEALPix map using the input CatSim stellar catalog to cross-correlate with our galaxy catalogs.
- Sky-background: We use the observed background level in each exposure and assign that value to the HEALPixel with $N_{side} = 2048$ that corresponds to the pointing position. After this we calculate the median value in each HEALPixel and use them to compute the cross-correlations with the galaxy catalogs. The caveat of this approach is that we are not propagating the geometry of the focal plane.
- Sky-noise: We use the observed noise background level in each exposure and proceed as in the previous case to build a HEALPix map with which we will cross-correlate.
- Seeing: We proceed as before and use the observed seeing in each exposure and build a HEALPix map.

These maps are shown in Figure A1 and Figure A2.

In the case of the real space measurements, we proceed the same way as ref. (Crocce et al. 2016) to compute the impact of the different potential sources for systematic uncertainty. We compute the auto and cross-correlations of these maps and our data samples to obtain the "true" correlation function:

$$w^{gg}(\theta)_{true} = w^{gg}(\theta)_{obs} - \vec{w}_{g,sys} \cdot W_{sys,sys}^{-1} \cdot \vec{w}_{g,sys} \tag{9}$$
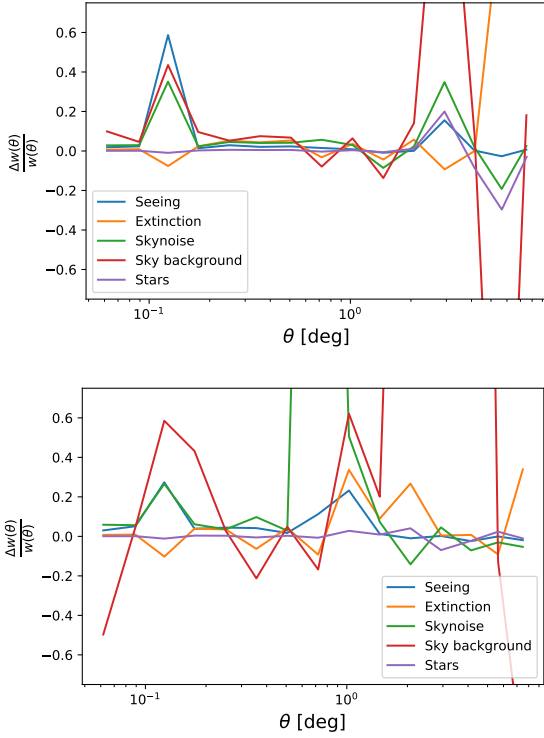
Where w_{true}^{gg} is the corrected galaxy-galaxy correlation function, w_{obs}^{gg} is the measured galaxy-galaxy autocorrelation, $\vec{w}_{g,sys}$ is the vector containing the cross-correlation between the galaxies and the different maps and $W_{sys,sys}^{-1}$ is the inverse of the matrix containing the cross-correlations between different systematics. For the stellar contamination we also follow the procedure presented in ref. (Crocce et al. 2016). Given a stellar fraction f_{star} the "true" galaxy correlation function is given by

$$w_{gal} = (1 + f_{star})^2 \left(w_{obs} - f_{star}^2 w_{sg} - \frac{f_{star}^4}{(1 + f_{star})^2}\right) \tag{10}$$

where w_{sg} is the cross-correlation between our stellar map and the observed galaxies.

Comparing with the input catalog we select those objects classified as galaxies whose centroids lie within 2 pixels

Figure 17. Results for the two-point correlation function in the input (green), dithered (blue) and undithered (orange) datasets. We can see that after the correction (triangles) for the systematic effects the agreement is better than without the correction (circles) between the input and output data especially for the undithered case (for the dithered case the corrections are negligible).

Figure 16. Correction due to the different potential sources of systematic uncertainty relative to the value of the measured correlation function of the dithered (top) and undithered (bottom) datasets.

of a star from the input catalog. From those, we select the objects that have a magnitude difference smaller than 30 mmags. Doing this we estimate a stellar contamination of $f_{star} = 7.2\%$ in our sample.

We compare the correction term for the different systematics to the measured signal obtaining the results in Figure 16, where we can appreciate that the dithering strategy is working reducing the impact of the systematics, keeping them under control and at percent level for this "small" area, improving the signal-to-noise in addition to other benefits explored in ref. (Awan et al. 2016). This is also seen Figure 17 where we clearly see that the uncorrected and corrected correlation function for the dithered field are essentially the same.

In the case of harmonic space we use the mode projection from `NaMaster` to correct for the different templates.**Add figure with corrected and uncorrected power-spectra.**

8.4 Pushing the dataset further

We also wanted to check what happens if we choose a sample where the uniformity across the footprint is still good even though completeness is not as good. We extended our sample by selecting galaxies with $16 < $ `CMODEL_MAG` $ < 26.25$ and depth≥ 26.25. This increases the sample from 4.3 million galaxies to 6.5 million in the dithered sample, even though the footprint is reduced by 8%. However, these selection cri-

teria reduce the number of galaxies to 4.2 million in the undithered sample, as well as the footprint by 35%.

9 CONCLUSIONS

In this paper we presented the methodology to characterize the transfer function of LSST. This methodology can be easily exported to different photometric surveys. First, we performed a quality assessment of the data produced by the pipeline. Then, we generated the mask to perform our clustering analyses. Finally we compared the input and output two point clustering statistics to characterize the transfer function. **Add more things when we have more results**.

REFERENCES

Awan, H., Gawiser, E., Kurczynski, P., et al. 2016, ApJ, 829, 50
Bosch, J., Armstrong, R., Bickerton, S., et al. 2017, ArXiv e-prints, arXiv:1705.06766
Bruderer, C., Chang, C., Refregier, A., et al. 2016, ApJ, 817, 25
Brun, R., Hagelberg, R., Hansroul, M., & Lassalle, J. C. 1978, Simulation program for particle physics experiments, GEANT: user guide and reference manual (Geneva: CERN)
Bruzual, G., & Charlot, S. 2003, MNRAS, 344, 1000
Cabré, A., Fosalba, P., Gaztañaga, E., & Manera, M. 2007, MN-RAS, 381, 1347
Crocce, M., Carretero, J., Bauer, A. H., et al. 2016, MNRAS, 455, 4301
De Lucia, G., Springel, V., White, S. D. M., Croton, D., & Kauff-mann, G. 2006, MNRAS, 366, 499

DESI Collaboration, Aghamousa, A., Aguilar, J., et al. 2016, ArXiv e-prints, arXiv:1611.00036

Dodelson, S. 2003, Modern cosmology (San Diego, CA: Academic Press)

Elsner, F., Leistedt, B., & Peiris, H. V. 2017, MNRAS, 465, 1847

Gonzalez, O. A., Rejkuba, M., Zoccali, M., Valenti, E., & Minniti, D. 2011, A&A, 534, A3

Górski, K. M., Hivon, E., Banday, A. J., et al. 2005, ApJ, 622, 759

Hivon, E., Górski, K. M., Netterfield, C. B., et al. 2002, ApJ, 567, 2

Ivezic, Z., Tyson, J. A., et al. 2008a, ArXiv e-prints, arXiv:0805.2366

Ivezic, Z., Tyson, J. A., Abel, B., et al. 2008b, ArXiv e-prints, arXiv:0805.2366

Jarvis, M., Bernstein, G., & Jain, B. 2004, MNRAS, 352, 338

Jurić, M., Ivezić, Ž., Brooks, A., et al. 2008, ApJ, 673, 864

Jurić, M., Kantor, J., Lim, K., et al. 2015, ArXiv e-prints, arXiv:1512.07914

Krisciunas, K., & Schaefer, B. E. 1991, PASP, 103, 1033

Landy, S. D., & Szalay, A. S. 1993, ApJ, 412, 64

LSST Dark Energy Science Collaboration. 2012, ArXiv e-prints, arXiv:1211.0310

LSST Science Collaboration. 2009, ArXiv e-prints, arXiv:0912.0201

Norberg, P., Baugh, C. M., Gaztañaga, E., & Croton, D. J. 2009, MNRAS, 396, 19

Pedregosa, F., Varoquaux, G., Gramfort, A., et al. 2011, Journal of Machine Learning Research, 12, 2825

Peterson, J. R., Jernigan, J. G., Kahn, S. M., et al. 2015, ApJS, 218, 14

Rowe, B. T. P., Jarvis, M., Mandelbaum, R., et al. 2015, Astronomy and Computing, 10, 121

Schlegel, D. J., Finkbeiner, D. P., & Davis, M. 1998, ApJ, 500, 525

Sérsic, J. L. 1963, Boletin de la Asociacion Argentina de Astronomia La Plata Argentina, 6, 41
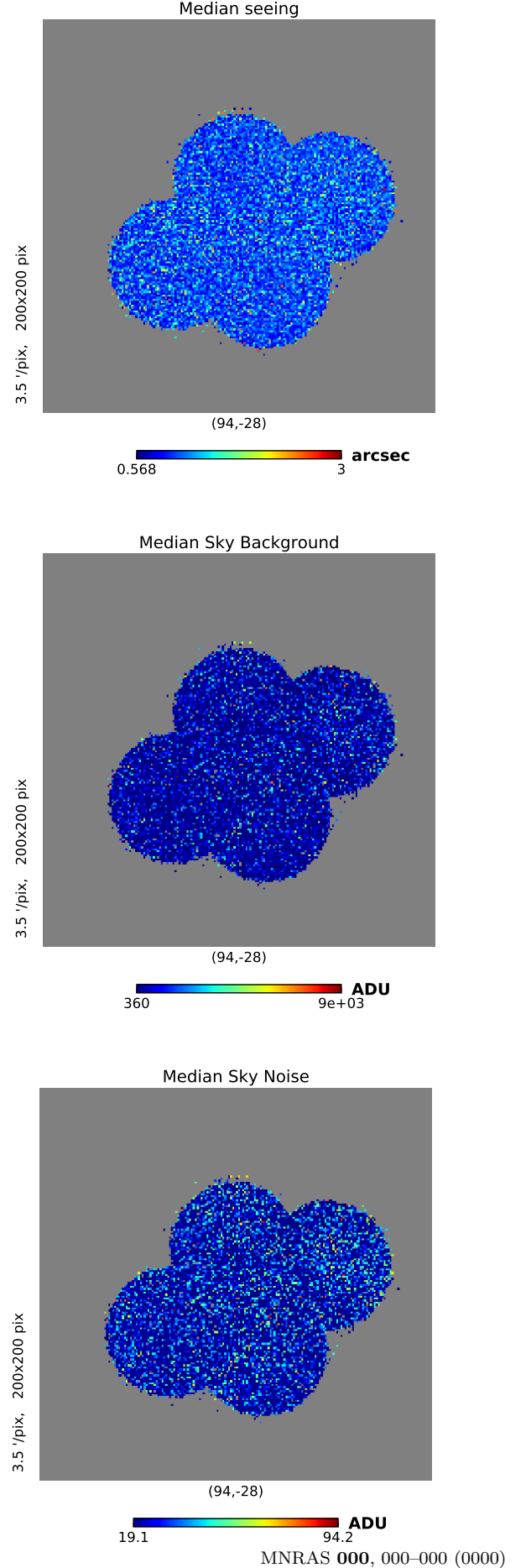
Shao, J. 1986, Annals of Statistics, 14, 1322

Sjöstrand, T., Mrenna, S., & Skands, P. 2006, Journal of High Energy Physics, 5, 026

Springel, V., White, S. D. M., Jenkins, A., et al. 2005, Nature, 435, 629
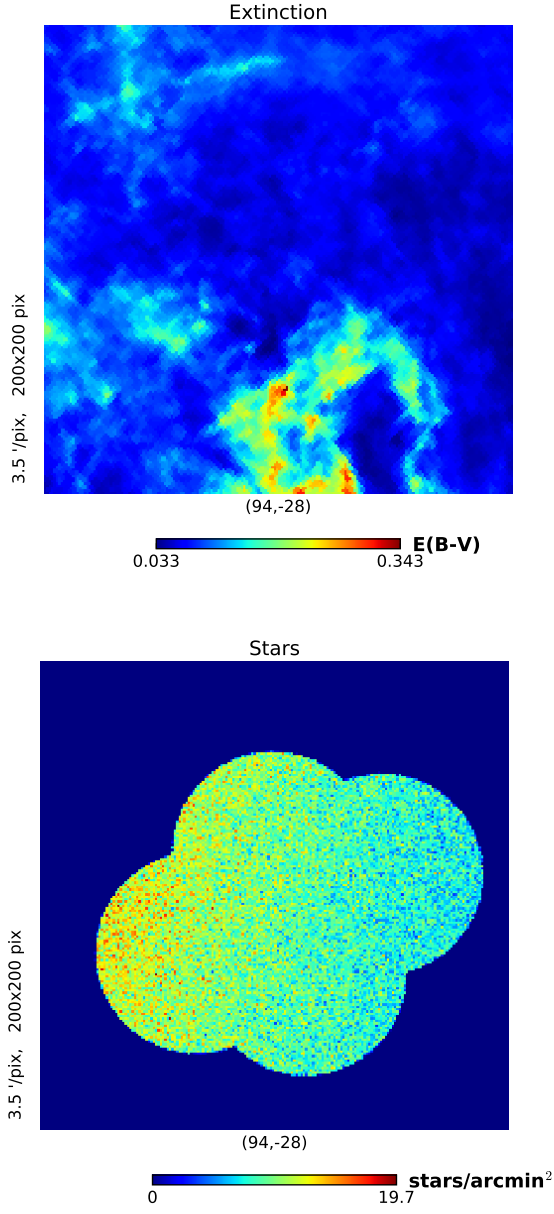
Springel, V., White, S. D. M., Jenkins, A., et al. 2005, Nature, 435, 629 EP

Suchyta, E., Huff, E. M., Aleksić, J., et al. 2016, MNRAS, 457, 786

APPENDIX A: MAPPING OBSERVATIONAL EFFECTS

Figure A1. HEALPix maps showing the different observational effects that might be potential cause of systematic uncertanties.

Figure A2. HEALPix maps showing the different observational effects that might be potential cause of systematic uncertanties.